Calibration of the Fermilab Booster ionization profile monitor

J. Amundson, J. Lackey, and P. Spentzouris
Fermi National Accelerator Laboratory, Batavia, Illinois 60510, USA

G. Jungman
Los Alamos National Laboratory, Los Alamos, New Mexico 87545, USA

L. Spentzouris
Department of Biological, Chemical, and Physical Sciences, Illinois Institute of Technology, Chicago, Illinois 60616, USA
(Received 20 May 2003; published 9 October 2003)

The booster ionization profile monitor (IPM) obtains transverse beam profiles by measuring the distribution of ions resulting from interaction of the proton beam with background gas in the beam chamber. The challenge of the IPM operation is that the measured ion distribution is not an exact representation of the beam distribution, since the ion trajectories are influenced by the electromagnetic field of the beam. We have developed a new model for the dependence of the IPM measurement on the beam parameters, assuming a Gaussian beam distribution. Our model of the ion dynamics in the detector was constrained by making independent measurements of the horizontal beamwidth at injection and extraction and comparing these to data taken from the IPM at the same time. Our calibration results in the formula $\sigma_{\text{measured}} = \sigma_{\text{real}} + C_1 N \sigma_{\text{real}}^{p_1}$, where N is the number of protons in the machine, in units of 10^{12}, $C_1 = (1.13 \pm 0.06) \times 10^{-5}$, in units of $(\text{meters})^{1-p_1}/10^{12}$, and $p_1 = -0.615 \pm 0.013$; the subscript "measured" indicates the raw IPM measurement, the subscript "real" the true beamwidth. This result is the first detailed calibration of the response of the booster IPM based on experimental data.

DOI: 10.1103/PhysRevSTAB.6.102801 PACS numbers: 41.85.Ew, 41.85.Qg

I. INTRODUCTION

The Fermilab Booster is a rapid cycling, 15 Hz, alternating-gradient synchrotron with radius of 75.47 m, that accelerates protons from 400 MeV kinetic energy to 8 GeV [1]. Multiturn H^- injection is used; the pulse duration of the injected linac beam is typically ten booster turns. In other words, the linac beam fills the booster ring circumference 10 times. During injection, a set of pulsed magnets (ORBUMP) produce a local orbit distortion used to superimpose the trajectories of the already circulating beam and the incoming injected beam. The stripping foil is located at the peak deflection of this orbit bump.

The booster ionization profile monitor (IPM) is the only device in the booster capable of measuring beam profiles with a time resolution of a single turn (2.2 μs at injection) at all times in the cycle. The IPM measures profiles using ions produced by the interaction of the beam with the imperfect vacuum of the machine. An applied transverse clearing field of 8 kV causes the ions to drift to a microchannel plate (MCP). The beam direction defines the longitudinal coordinate. The detector is 0.5 m long, with a transverse gap of 12 cm. The MCP plate is $8 \times 10\ \text{cm}^2$ and has strip spacing 1.5 mm [2,3]. The response of the IPM depends on the charge of the beam and so must be calibrated as a function of the injected number of protons.

To calibrate the IPM response, we compared the beam profiles obtained with the IPM against independent beam profile measurements. These measurements were obtained at injection, using a single wire, and at extraction, using a multiwire proportional chamber in the extraction line MI-8. In order to obtain few-turn resolution during the injection measurements, we utilized a new technique where the beamwidth is measured using a stationary wire at the location of the injection bump. The beam traverses this wire as the ORBUMP field decays at the end of the linac beam pulse.

II. THEORETICAL CALCULATION

Our objective is to measure the projection of the beam distribution on each one of the transverse coordinates. For an ideal measurement of one projection, the ions' drift should be parallel to the other (nonmeasured) coordinate. For this purpose, the IPM provides an external field which is applied to the beam along the nonmeasured coordinate. On the other hand, the field due to the beam itself is radial, so it affects the motion of the ions in both planes, distorting the ion profile from an ideal match to the beam profile. Figure 1 displays sample trajectories of ions in the IPM with and without the presence of the beam-induced field. The simulation used to calculate the trajectories is described in Sec. III. We now calculate the distortion created by the beam's self-field.

We start by considering the scattering of particles of a beam with a Gaussian transverse profile caused by the field generated by the beam itself as well as an applied electric field. The total force felt by an ion in the combined field is

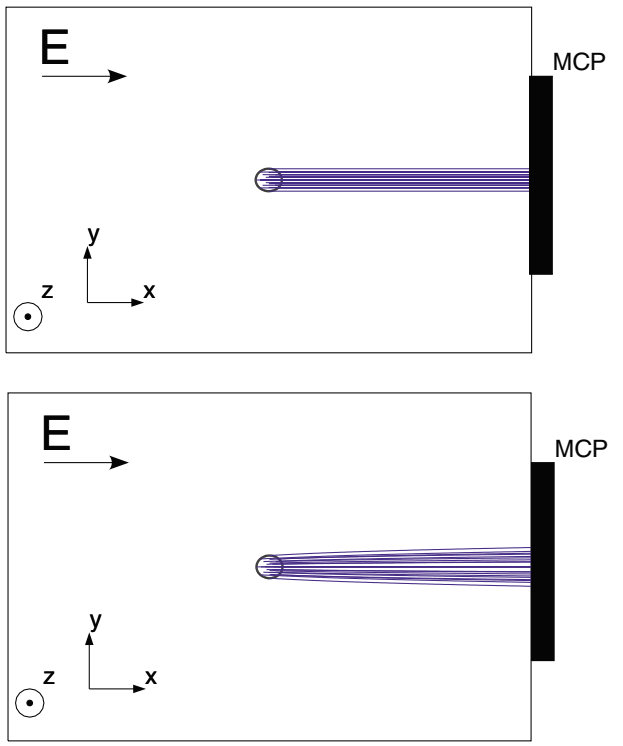

FIG. 1. (Color) Simulated ion trajectories in the IPM. Ions are created by the beam (traveling in the $+z$ direction) in the center, then drift toward the MCP. The upper diagram is the idealized case where the field due to the beam is negligible. The lower diagram shows the distortion of the trajectories for realistic beam parameters.

$$\vec{F} = \hat{r}\frac{a}{r}[1 - \exp(-r^2/2\sigma^2)] + b\hat{x}, \tag{1}$$

where $\hat{r}$ and $\hat{x}$ are unit vectors in the radial and x directions, respectively. Here σ is the total transverse rms width of the beam distribution. The coefficient a is proportional to N, the number of protons in the booster, which we will typically measure in units of 10^{12}. The external field is perpendicular to the coordinate in which we are measuring the beam profile. The longitudinal coordinate (z) is the beam direction. We ignore the curvature of the beam in the longitudinal direction since the size of the detector is small compared to the circumference of the ring. This calculation assumes a dc beam. The actual booster beam is effectively dc near injection, then it is bunched during the cycle. The applied field in the IPM is small enough that an ion sees several bunches before it has traveled one σ of the beam distribution and tens of bunches before it reaches the readout. A dc beam is therefore a reasonable approximation throughout the booster cycle. A discussion of the effects of beam bunching versus the IPM's applied electric field can be found in Ref. [4].

It is instructive to compare the relative magnitudes of the applied field and the field due to the beam. A typical beam at extraction might have $\sigma = 2.0$ mm and $N = 2.5 \times 10^{12}$. Then

$$\frac{\frac{a}{r_{\max}}[1 - \exp(-r_{\max}^2/2\sigma^2)]}{b} \simeq \frac{1}{24}, \tag{2}$$

where $r_{\max}$ is the distance from the center of the beam at which the field due to the beam is maximum. The small value of this ratio suggests that it makes sense to start by ignoring the field due to the beam, then reintroduce it as a perturbation.

It is possible to analytically calculate the average absolute deflection in the y coordinate due to the scattering by the above force to leading order in the small parameter a, or, equivalently, the current N. The result is

$$\langle|y_{\text{out}}|\rangle = \langle|y_{\text{in}}|\rangle + KN\sigma_{\text{real}}^{-1/2}, \tag{3}$$

where y_{in} is the initial y coordinate of the ion and y_{out} is the y coordinate of its arrival at the MCP. In the absence of beam self-field effects, the above equation reduces to $y_{\text{in}} = y_{\text{out}}$, i.e., there is no distortion in the profile measurement.

The constant K is a complicated integral involving the forces and distributions in the problem, but independent of the parameters σ_{real} and N. We assert without proof that the scaling behavior above is insensitive to the detailed shape of the beam distribution. Different beam shapes can only modify the size of K. The value of K also depends on the details of the IPM such as the distribution of ions, distance to the wall, etc. We will include details and a calculation of the variance of y in a full paper.

III. SIMULATIONS AND PHENOMENOLOGY

We have written a two-dimensional simulation of the physics of the preceding section using OCTAVE [5]. In the simulation we distribute particles in the x-y plane according to an x/y-symmetric Gaussian distribution of width σ_{real}. We then calculate the individual particle trajectories using the force given in Eq. (1). Finally, we calculate the y location of the intercept of each particle trajectory with the MCP and form a histogram of the intercepts. Figure 1 shows some typical trajectories obtained from our simulation. In the actual booster IPM, the width of the distribution is determined from a fit to a Gaussian plus a linear background. We followed the same procedure in the simulation, even though the background in the input distribution is zero in order to best match the fitting procedure used in the actual IPM. The resulting fitted width, σ_{smeared}, is our estimate of the σ_{measured} observed in the actual IPM.

The parameters of the simulation include the geometry of the IPM, the strength of the clearing field, and the beamwidth and current. These parameters are all well determined. In order to understand the time resolution of the detector, one additional parameter is needed: the mass of the ions themselves. However, the spatial

smearing due to the beam charge is independent of the ion mass [4]. In our simulation, we take the mass to be the mass of a water molecule. A distribution of ions of different species is present in the actual beam pipe [6].

Our simulation is similar to the simulation described in Graves' thesis [3], the first use of the booster IPM for emittance measurements. Since the computer power available to us now is substantially greater than what was available for Graves' original work, we have been able to extend our simulations of a larger range of parameter space and to work to higher accuracy. In Fig. 2 we show the results of our simulation, as well as the results of Graves' earlier work. Our new simulation closely matches the original simulation in the region of overlap.

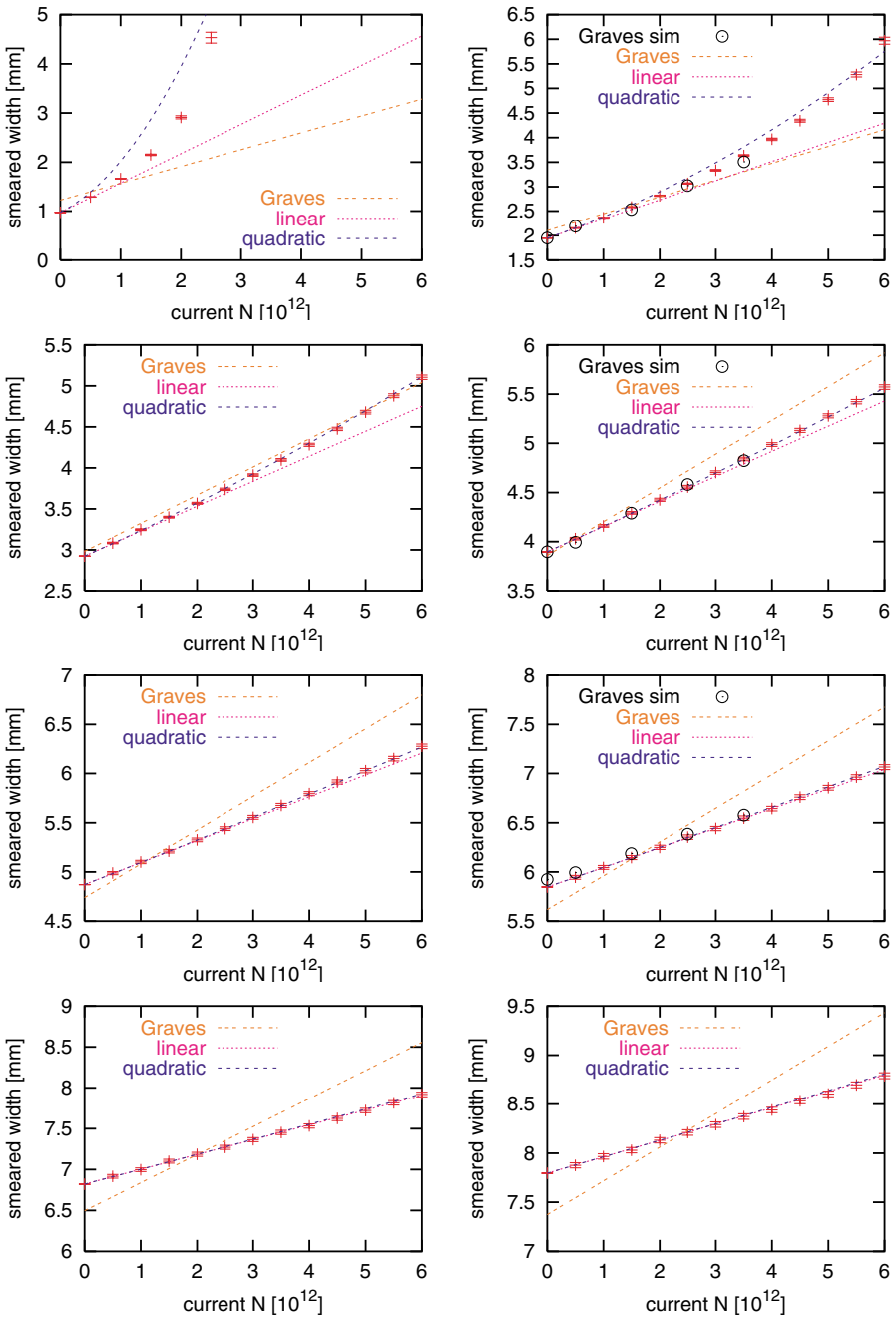

FIG. 2. (Color) Simulations and parametrizations. The crosses are the results of our OCTAVE simulation, including error bars. The circles are the results of the simulation in Graves' thesis, for which no error bars are available. The smeared width is the width that would be observed in the IPM under the assumptions of our model, and it is plotted versus the beam current, in units of 10^{12} protons per turn. Each one of the plots corresponds to a different initial value of σ_{real}, the value which corresponds to zero current. The linear and quadratic forms used to parametrize the response of the IPM are described in the text, as is the Graves parametrization.

In Ref. [3], the following formula is used to parametrize the results of simulations

$$\sigma_{\text{real}} = \tilde{C}_1 + \tilde{C}_2\sigma_{\text{measured}} + \tilde{C}_3 N. \quad (4)$$

This formula is currently implemented in the booster IPM data collection system [2] to estimate the real beamwidth from the measured distribution. The simplest physical observation we can make about the scaling of measured versus real beamwidths is that

$$\sigma_{\text{measured}} \to \sigma_{\text{real}} \quad \text{as } N \to 0. \quad (5)$$

Unfortunately, the simple parametrization above does not have this property. Inspired by the theoretical result of the previous section, we try the parametrization

$$\sigma_{\text{measured}} = \sigma_{\text{real}} + C_1 N \sigma_{\text{real}}^{p_1}, \quad (6)$$

which we refer to as the linear (in N) parametrization. Postulating the form of the next term in the expansion, we also consider the quadratic form

$$\sigma_{\text{measured}} = \sigma_{\text{real}} + C_1 N \sigma_{\text{real}}^{p_1} + C_2 N^2 \sigma_{\text{real}}^{p_2}. \quad (7)$$

Validating the linear and quadratic parametrizations is complicated by the fact that there are two independent variables, σ_{real} and N. We tested these parametrizations by performing two stages of fitting to the results of the simulation. First, we fit a parabola to the quantity $\sigma_{\text{measured}} - \sigma_{\text{real}}$, where σ_{measured} is the smeared σ predicted by the simulation, for each fixed σ_{real} using N as the independent variable. Next, we plot the coefficients of the parabolic fit as a function of σ_{real}. If the linear and quadratic parametrizations describe the simulation well, the coefficients of the first parabolic fits should be described by power laws. The plots of the coefficients, along with power-law fits, are shown in Fig. 3. The fitted parameters are shown in Table I. Returning to Fig. 2, we see that the power-law fit with the linear term alone is sufficient for most of the parameter space we explored. It is only in a region where σ_{real} becomes small and N becomes large that the quadratic term in the power-law fit becomes important. Even with the quadratic term, beam sizes around 1 mm are not well described by our parametrizations, linear or quadratic. However, beams as small as 1 mm are never observed in the booster under normal operating conditions.

The extracted value $p_1 = -0.615 \pm 0.013$ is similar to, but not exactly the same as, the value $-\frac{1}{2}$ obtained in the calculation of Sec. II. In the calculation we estimated the overall linear spread in the measured y, $\langle|y_{\text{out}}|\rangle$. In the simulation, however, we extracted widths by fitting to a Gaussian with a linear background, as described above. We expect the behavior of $\langle|y_{\text{out}}|\rangle$ to be similar to, but not exactly the same as the width obtained from the fitting procedure. The small difference in the powers is therefore not unexpected.

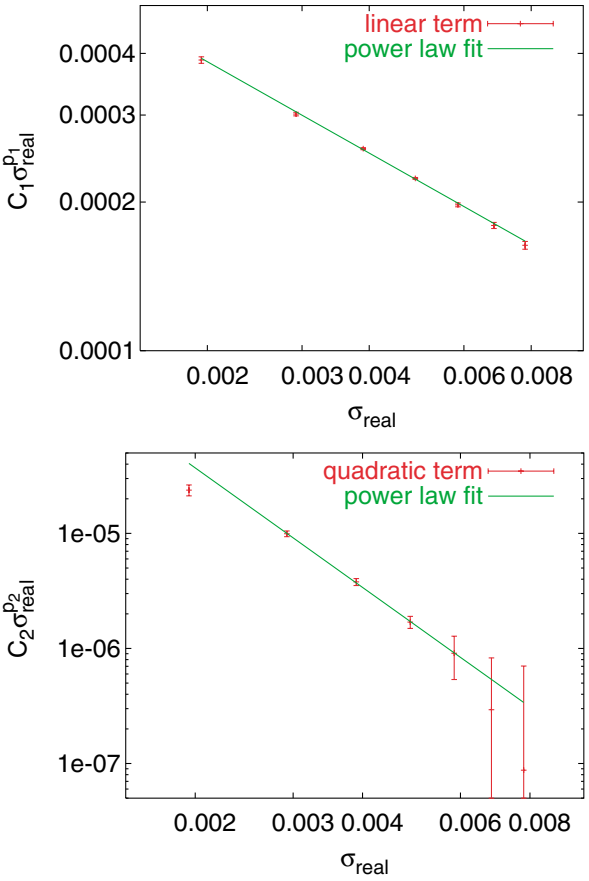

FIG. 3. (Color) Power-law fits to parabolic coefficients as described in the text. The smallest value of σ_{real} was left out of the quadratic term fit to avoid contamination from higher-order terms in the series.

TABLE I. Results from fits to our simulation for linear and quadratic parametrizations.

Parameter	Fitted value	Uncertainty	Units
C_1	8.44×10^{-6}	0.61×10^{-6}	$\text{m}^{1-p_1}/10^{12}$
p_1	-0.615	0.013	None
C_2	1.8×10^{-14}	1.3×10^{-14}	$\text{m}^{1-p_2}/10^{24}$
p_2	-3.45	0.12	None

IV. MEASUREMENTS

In order to obtain an experimental measure of the IPM calibration, we took width measurements simultaneously with the booster IPM, the MI-8 extraction line wire chamber and the so-called "flying beam" wire. The flying beam wire is a single wire measuring device located in the booster injection area at a straight section, long 1, which can be positioned just outside the beam envelope of the injected beam, i.e., beam envelope with the ORBUMP magnets on. At injection, the ORBUMP magnets keep the beam trajectory displaced by ~4 cm with respect to the nominal beam orbit, so that the injected H^- ions will pass

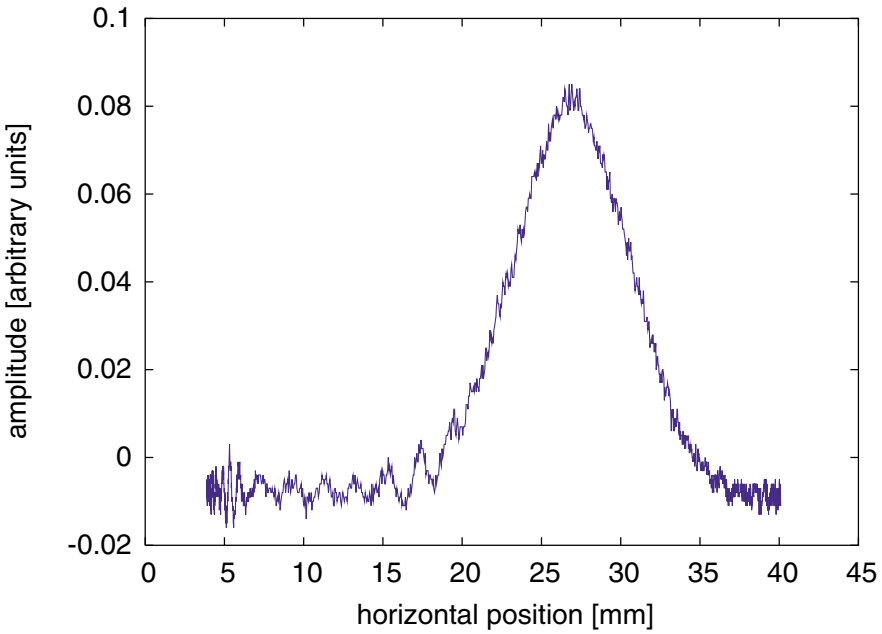

FIG. 4. (Color) Typical horizontal beam profile measured with the "flying beam" wire.

through a stripping foil. The wire is placed between the displaced and nominal orbits. As the ORBUMP current decays, the beam sweeps through the wire, providing a measure of the horizontal beam profile. The time resolution of the wire measurements is determined by the duration of the ORBUMP current decay, which is roughly five turns. By recording the ORBUMP current as a function of time, $I(t)$, and the response of the wire as a function of time, $a(t)$, we can reconstruct the horizontal profile, $a(x)$, as measured by the wire by using the known beam position as a function of current, $x(I)$. See Fig. 4 for a display of a typical beam profile as measured by the flying beam wire.

The turn number for which we extract the profile is controlled by the timing of the injected beam relative to the ORBUMP current pulse; injecting a beam closer to the falling edge of the magnet pulse gives an earlier turn number. The range of turns for which we can extract beam profiles with this technique is thus limited by the length of the ORBUMP pulse, which amounts to roughly 30 turns. There is a drawback in this method: we can measure only one profile during a given booster cycle. If we want to measure widths of different turn numbers, we are only able to do so during different booster cycles. Also, since the ORBUMP affects only the horizontal plane, we can only directly calibrate the horizontal IPM detector. The vertical detector can be calibrated by temporarily rotating it to the horizontal plane.

After injection into the booster, the transverse size of the beam decreases during acceleration. Since the flying beam wire measures beamwidths during the first few turns and the MI-8 chamber measures the beamwidth after extraction, we were able to see the extremes of the range of beam sizes available. We varied the beam intensity between 1 and 13 injected turns in order to explore a wide variety of intensities as well. For the analysis presented here we used data sets collected on November 11, 2002 and December 10, 2002.

In order to directly compare data from different locations in the booster, the widths obtained from the wire-based detectors were scaled according to the values of their β functions relative to the β function at the IPM location. The scaling for the wire is $\sigma_{\text{wire@IPM}} = \sqrt{\beta_{\text{IPM}}/\beta_{\text{wire}}} \times \sigma_{\text{wire}} \approx 0.93 \times \sigma_{\text{wire}}$, where $\beta_{\text{IPM}} = 5.73$ m and $\beta_{\text{wire}} = 6.63$ m at injection [7]. The scaling for the chamber is $\sigma_{\text{cham@IPM}} = \sqrt{\beta_{\text{IPM}}/\beta_{\text{chamber}}} \times \sigma_{\text{chamber}} \approx 0.82 \times \sigma_{\text{chamber}}$, where $\beta_{\text{chamber}} = 17.97$ m at extraction [8]. The raw data are summarized in Tables II and III. Also, since the time resolution of the flying beam wire is roughly five turns, we average the IPM measured beam profiles from five consecutive turns to compare with the wire. Examples of horizontal beam profiles as measured by the IPM for three different beam intensities are shown in Fig. 5.

In comparing our experimental results with the simulations, we found that all of the data fell in the regime in which the linear and quadratic power-law fits were indistinguishable. As a simple test of the power-law scaling seen in the simulation, we plot the quantity $(\sigma_{\text{measured}} - \sigma_{\text{real}})/N$ as a function of σ_{real} for all of the data and simulation points. We take σ_{real} to be the width obtained from the wire or chamber and σ_{measured} to be the raw (uncorrected) width obtained from the IPM. The simulation points for a given value of σ_{real} will fall on top of each other only to the degree that the linear power-law fit is sufficient to describe the simulation. Since we argued

TABLE II. Wire ("flying beam") data. The IPM and wire widths are extracted by a fit to the corresponding profile data using Gaussian plus a first degree polynomial function.

Charge (10^{12})	Fit width from wire	Error on wire width	Fit width from IPM	Error on IPM width	No. IPM points
0.550	3.1100	0.0928	4.552	0.291	20
0.981	3.2375	0.1064	4.288	0.106	43
1.258	3.8882	0.0017	4.393	0.024	17
2.085	3.8305	0.0035	5.053	0.099	17
3.158	3.7846	0.0053	5.273	0.060	11
3.295	3.8057	0.0015	4.868	0.046	11
3.439	4.0525	0.0012	5.445	0.103	7
4.425	3.9399	0.0045	5.158	0.055	12
5.030	3.7570	0.0072	6.406	0.118	15
6.450	3.8778	0.0042	6.532	0.096	10

TABLE III. MI-8 chamber data. The IPM width is extracted by a fit to the IPM profile data using a Gaussian plus a first degree polynomial function.

Charge (10^{12})	rms width from chamber	Error on chamber width	Fit width from IPM	Error on IPM width	No. IPM points
0.800	2.045	0.081	2.604	0.047	43
1.562	2.168	0.041	2.995	0.065	17
2.341	2.250	0.041	3.327	0.039	11
3.135	2.370	0.041	3.744	0.035	12
4.053	2.618	0.041	4.276	0.037	7
4.200	3.300	0.050	4.906	0.100	35

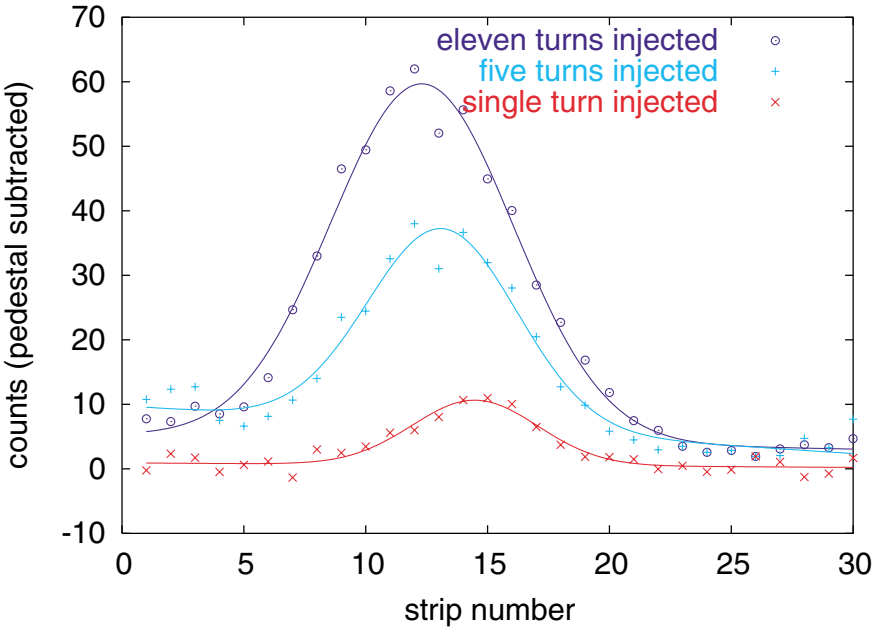

FIG. 5. (Color) IPM measured horizontal beam profiles for a beam charge of one (red line), five (cyan line), and eleven (blue line) injected turns in the machine. The corresponding lines are a fit to the data using a Gaussian plus a first degree polynomial function.

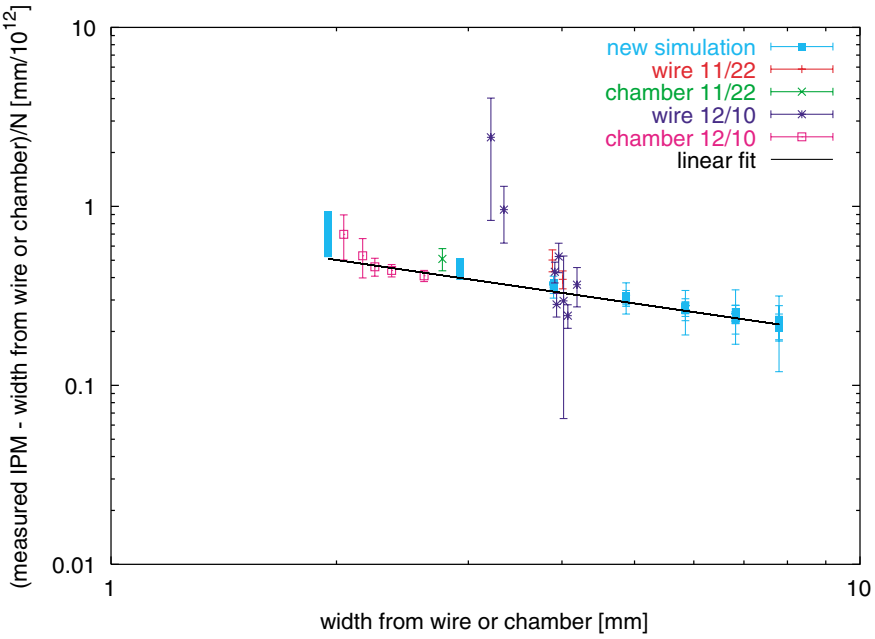

FIG. 6. (Color) Comparison of our linear parametrization with the data and simulation. The linear parametrization predicts a linear relationship between the quantities plotted. The simulation has been normalized to match the data.

that the constant C_1 depends on the details of the beam and IPM, we let it float in order to find the best fit to the data. We did not vary the parameter p_1. The value of C_1 we get from the fit to the data, $(1.13 \pm 0.06) \times 10^{-5}\ \mathrm{m}^{1-p_1}/10^{12}$, is approximately one-third larger than the value we obtained from the simulation (see Table I), which is reasonable given the simple assumptions present in the model. Figure 6 shows the scaling behavior of the simulation is quite consistent with the data. Since we have not identified all the sources of systematic errors in the wire measurements we estimate their size from the scatter of the points of Tables II and III. This results in a total error which is approximately 3 times the size of the statistical error; the total error is shown in Fig. 6.

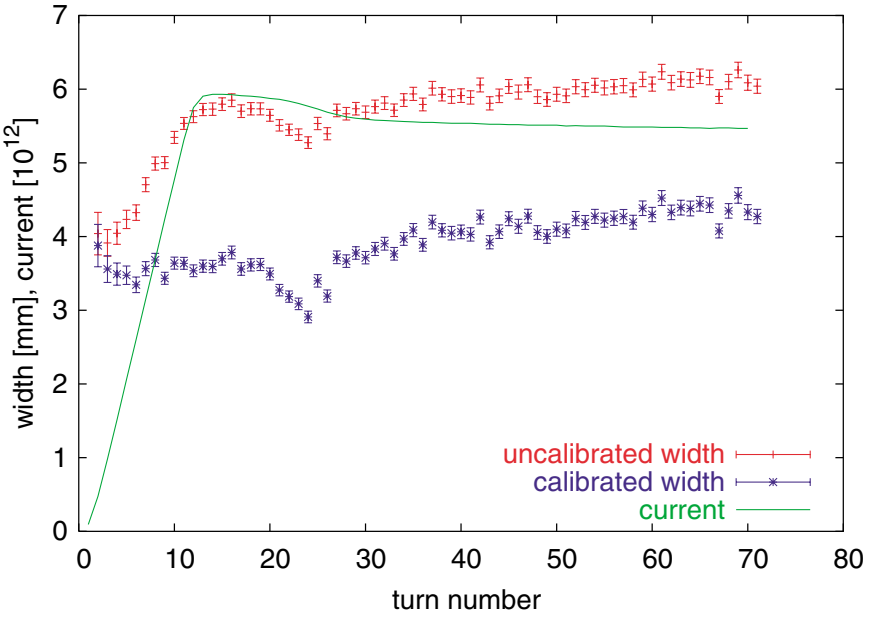

FIG. 7. (Color) Horizontal beamwidth in the booster, measured by the IPM as a function of time, measured in booster turns (2.2 μs), at injection. Both the calibrated (blue) and uncalibrated (red) widths are shown. Also shown (green curve) is the beam current in the machine, in units of 10^{12} protons/turn, versus time.

V. SUMMARY AND CONCLUSIONS

We have obtained a calibration for the FNAL Booster horizontal IPM detector, using a new device, the flying beam wire, at injection, and a multiwire proportional chamber at extraction. The data from these devices were compared to IPM measurements for different injected currents in the machine, and the IPM response was fit to a function determined by a two-dimensional electrodynamics model of the detector. We have found that the relation between the raw beamwidth seen in the IPM and the real width is well described by the function

$$\sigma_{\text{measured}} = \sigma_{\text{real}} + C_1 N \sigma_{\text{real}}^{p_1}, \tag{8}$$

where N is the current in units of 10^{12} protons in the machine, $C_1 = (1.13 \pm 0.06) \times 10^{-5}\ \text{m}^{1-p_1}/10^{12}$, and $p_1 = -0.615 \pm 0.013$. The range of validity in $(\sigma_{\text{real}}, N)$ can be extended by adding a term quadratic in N, but we do not find it necessary in order to reproduce our data.

The importance of the calibration for the booster IPM detector and the size of the beam self-field induced effects is demonstrated in Fig. 7, where both the calibrated and uncalibrated IPM beam profiles are shown, together with the beam current, as a function of time. The effect is most dramatic during the first 11 turns in the machine (injection time), since the beam current is changing. The change of the uncalibrated beamwidth clearly tracks the beam current change. The calibrated width shows a much smaller variation during the injection period.

ACKNOWLEDGMENTS

We would like to thank Stephen Pordes and James Zagel for useful discussions. This work was partially performed under the auspices of a Scientific Discovery through Advanced Computing project, "Advanced Computing for 21st Century Accelerator Science and Technology," which is supported by the US DOE/SC Office of High Energy and Nuclear Physics and the Office of Advanced Scientific Computing Research.

[1] E. Hubbard *et al.*, Fermilab Technical Memo No. TM-405, 1973. The booster injection energy was increased to 400 MeV in 1990, see "Fermilab Linac Upgrade Conceptual Design," Fermilab Memo, Fermilab-LU-Conceptual Design, 1989.

[2] J. Zagel, J. R. Chen, and D. Crisp, in *Fermilab Booster Ion Profile Monitor System Using LabVIEW—1994*, Proceedings of the Beam Instrumentation Workshop, AIP Conf. Proc. No. 333 (AIP, New York, 1994), pp. 384–390.

[3] W. S. Graves, Ph.D. thesis, University of Wisconsin, Madison, 1994.

[4] R. E. Thern, in *Proceedings of the 1987 Particle Accelerator Conference* (IEEE, New York, 1987), pp. 646–648.

[5] J. W. Eaton, GNU OCTAVE Manual, Network Theory Ltd., 2002, http://www.octave.org/

[6] Gas spectrometer measurements show that the residual gas composition includes molecules ranging from Ar to H_2, W. Pellico (private communication). Unfortunately, no such measurements have been published.

[7] A. Drozhdin, Booster Lattice Version 1.7, available at http://www-bd.fnal.gov/pdriver/booster/database.html

[8] Ming-Jen Yang, MI-8 line lattice function measurements (private communication).